



Insights into the Electrodeposition of Bi₂Te₃

Marisol S. Martín-González,^a Amy L. Prieto,^a Ronald Gronsky,^b Timothy Sands,^b
and Angelica M. Stacy^{a,z}

^aDepartment of Chemistry and ^bDepartment of Materials Science and Engineering, University of California, Berkeley, Berkeley, California 94720, USA

In this paper, the processes associated with the electrodeposition of bismuth telluride (Bi₂Te₃), a thermoelectric material, are reported along with an analysis of the composition and crystallinity of the resulting films. The electrodeposition can be described by the general reaction $3\text{HTeO}_2^+ + 2\text{Bi}^{3+} + 18\text{e}^- + 9\text{H}^+ \rightarrow \text{Bi}_2\text{Te}_3 + 6\text{H}_2\text{O}$. Cyclic voltammetry studies of Bi, Te, and Bi/Te dissolved in 1 M HNO₃ reveal two different underlying processes depending on the deposition potential. One process involves the reduction of HTeO_2^+ to Te^0 and a subsequent interaction between reduced Te^0 and Bi^{3+} to form Bi₂Te₃. A second process at more negative reduction potentials involves reduction of HTeO_2^+ to H_2Te followed by the chemical interaction with Bi^{3+} . Both processes result in the production of crystalline Bi₂Te₃ films in the potential range $-0.1 < E < -0.52$ V vs. Ag/AgCl (3 M NaCl) on Pt substrates as determined by powder X-ray diffraction (XRD). Electron probe microanalyses and XRD reveal that the films are bismuth-rich and less oriented for more negative deposition potentials.

© 2002 The Electrochemical Society. [DOI: 10.1149/1.1509459] All rights reserved.

Manuscript submitted October 17, 2001; revised manuscript received April 12, 2002. Available electronically September 18, 2002.

Solid-state thermoelectric devices convert thermal energy from a temperature gradient into electrical energy (the Seebeck effect) or electrical energy into a temperature gradient (the Peltier effect). Thermoelectric power generators are used most notably in spacecraft power generation systems (for example, in Voyager I and II)^{1,2} and in thermocouples for temperature measurement, while thermoelectric coolers are largely used in charge coupled device (CCD) cameras, laser diodes, microprocessors, blood analyzers, and portable picnic coolers.^{1,2} Thermoelectric coolers (also known as Peltier coolers) offer several advantages over conventional systems. As solid-state devices, they have no moving parts. They use no ozone-depleting chlorofluorocarbons, potentially offering a more environmentally responsible alternative to conventional refrigeration. Although some large-scale applications have been considered (on submarines and surface vessels), their efficiency is low compared to conventional refrigerators.

Scientific and technological interest in the production of nanostructured thermoelectric materials has been driven by recent theoretical studies, which suggest that quantum confinement of electrons and holes could enhance the efficiency of these materials significantly above that of their bulk values.³⁻⁵ This hypothesis has already been verified for thin multilayers of PbTe/Pb_{1-x}Eu_xTe.⁶⁻¹¹ Larger enhancements are predicted for one-dimensional (1-D) systems (nanowires) compared to 2-D systems (thin films).^{12,13} These predictions have stimulated research into the preparation of nanowires of thermoelectric materials.

Bismuth telluride (Bi₂Te₃) and its doped derivative compounds are considered to be the best materials to date for near room-temperature thermoelectric applications.^{14,15} The maximum figure of merit (ZT) occurs for optimized doping levels¹⁶ at approximately 70°C with an effective operating range of -100 to +200°C. Other attractive properties of this material at 21°C are its density (7530 kg/m³), its thermal conductivity (1.5 W/m K), its specific heat (544 J/kg K), and its thermal expansion coefficient (TEC, 13.0 × 10⁻⁶/°C). Therefore, Bi₂Te₃ is an excellent candidate material for the preparation of nanowires for thermoelectric applications.

The electrodeposition of Bi₂Te₃ is a fast, simple, and low cost synthetic method,¹⁷⁻²⁵ and a good choice for the fabrication of nanowires. However, the processes involved in the electrodeposition of Bi₂Te₃ are not very well understood. The overall reaction responsible for the deposition from aqueous acidic solutions has been described as¹⁸⁻²⁴



Although this is the general reaction, the processes involved in the deposition are much more complicated. In order to control the electrodeposition of nanostructures, it is important to understand these processes fully.

Here we report the Pourbaix diagram for Bi₂Te₃ along with a study of the deposition processes as determined by analyses of cyclic voltammograms (CVs) of solutions containing Bi and Te individually as well as solutions containing a mixture of both. In addition, Bi₂Te₃ films were prepared by electrodeposition at several potentials. The composition and crystallinity of these films were determined by electron probe microanalysis, scanning electron microscopy (SEM), and powder X-ray diffraction (XRD).

Experimental

Possible reactions relating various aqueous bismuth and tellurium species, and precipitates for this system are summarized in Table I, Eq. t.1 to t.36.²⁶ The standard electrode potential, E^0 , with respect to a normal hydrogen electrode (NHE) was calculated for each reaction by applying the Gibb's equation.²⁷ The Nernst equations showing the relationship between concentrations and either E^0 or pH given in Table I were used to calculate which species are most favorable for a particular pH and potential. With this information, a Pourbaix diagram (pH vs. potential) was calculated for Bi₂Te₃ under our experimental conditions for the electrodeposition of Bi₂Te₃, namely, Te (1×10^{-2} M) and Bi (0.75×10^{-2} M) dissolved in 1 M HNO₃ at 25°C.

CVs were recorded with a Bioanalytical Systems Basomatic CV50W unit. A three-electrode electrochemical cell was employed consisting of a Ag/AgCl reference electrode (3 M NaCl, 0.175 V vs. NHE), a Pt disk working electrode and a Pt wire counter electrode. The working electrode was polished and ultrasonically cleaned before each voltammogram in order to ensure a clean surface for each scan. Voltammograms were recorded at different scan rates (between 1 and 50 mV/s) and multiple scans were done for each scan rate. Typical scans performed at 10 mV/s are shown for comparative purposes throughout this paper. The potential limits for the voltammograms were established by scanning first from 2 to -2 V to determine the solvent window and the oxidation/reduction potentials.

The solutions studied were (i) Bi³⁺ (0.75×10^{-2} M); (ii) HTeO_2^+ (1×10^{-2} M); and (iii) HTeO_2^+ (1×10^{-2} M) plus Bi³⁺ (0.75×10^{-2} M). Concentrated nitric acid (Fisher, 69.1%) was used to dissolve the elements, and then the solution was diluted to 1

^z E-mail: astacy@socrates.berkeley.edu

Table I. Thermodynamic expressions for the Bi₂Te₃ system. Electrode reactions and their corresponding potentials are quoted vs. the normal hydrogen electrode at 25°C.

	Reaction	Potential or pH expression
a.	$H_2 \rightarrow 2H^+ + 2e^-$	$E^0 = 0.000 - 0.0591 \text{ pH}$
b.	$2H_2O \rightarrow O_2 + 4H^+ + 4e^-$	$E^0 = 1.228 - 0.0591 \text{ pH}$
t.1.	$Bi_2Te_3 + 6H_2O \rightarrow 3HTeO_2^+ + 2Bi^{3+} + 18e^- + 9H^+$	$E^0 = -0.62 - 0.01475 \log[HTeO_2^+] + 0.0443 \text{ pH}$
t.2.	$BiH_3 \rightarrow Bi + 3H^+ + 3e^-$	$E^0 = -0.800 - 0.0591 \text{ pH} - 0.0197 \log P_{BiH_3}$
t.3.	$H_2Te \rightarrow Te + 2H^+ + 2e^-$	$E^0 = -0.717 - 0.0591 \text{ pH} - 0.0295 \log P_{H_2Te}$
t.4.	$Bi_2Te_3 + 12H_2O \rightarrow 3TeO_3^{2-} + Bi_2O_3 + 18e^- + 24H^+$	$E^0 = -0.72 - 0.0098 \log[TeO_3^{2-}] + 0.0786 \text{ pH}$
t.5.	$2HTe^- \rightarrow Te_2^{2-} + 2H^+ + 2e^-$	$E^0 = 0.795 - 0.0591 \text{ pH} + 0.0295 \log \frac{[Te_2^{2-}]}{[HTe^-]^2}$
t.6.	$2Te^{2-} \rightarrow Te_2^{2-} + 2e^-$	$E^0 = 1.445 + 0.0295 \log \frac{[Te_2^{2-}]}{[Te^{2-}]^2}$
t.7.	$H_2Te \rightarrow HTe^- + H^+$	$\text{pH} = 3.37 - \log \frac{P_{H_2Te}}{[HTe^-]}$
t.8.	$HTe^- \rightarrow Te^{2-} + H^+$	$\text{pH} = 11.00 + \log \frac{[Te^{2-}]}{[HTe^-]}$
t.9.	$Bi_2Te_3 + 6H^+ + 6e^- \rightarrow 3Te + 2BiH_3$	$E^0 = -0.6673 - 0.0197 P_{BiH_3} - 0.0591 \text{ pH}$
t.10.	$\frac{3}{2} Te_2^{2-} + 2Bi \rightarrow Bi_2Te_3 + 3e^-$	$E^0 = 1.106 + 0.0295 \log[Te_2^{2-}]$
t.11.	$Bi_2Te_3 \rightarrow 3Te^{4+} + 2Bi^{3+} + 18e^-$	$E^0 = -0.52 - 0.00328 \log[Te^{4+}]^3[Bi^{3+}]^2$
t.12.	$Bi_2Te_3 + 6H_2O \rightarrow 3TeO_2 + 2Bi^{3+} + 18e^- + 12H^+$	$E^0 = -0.502 - 0.0066 \log[Bi^{3+}] + 0.0394 \text{ pH}$
t.13.	$Bi_2Te_3 + 8H_2O \rightarrow 3TeO_2 + 2BiOH^{2+} + 18e^- + 14H^+$	$E^0 = -0.513 - 0.0066 \log[BiOH^{2+}] + 0.046 \text{ pH}$
t.14.	$Bi_2Te_3 + 9H_2O \rightarrow 3TeO_2 + 2Bi_2O_3 + 18e^- + 18H^+$	$E^0 = -0.522 - 0.0591 \text{ pH}$
t.15.	$TeO_3 \rightarrow H_2O \rightarrow HTeO_4^- + H^+$	$E^0 = 6.17 + \log[HTeO_4^-]$
t.16.	$Te^{4+} + 2H_2O \rightarrow HTeO_2^+ + 3H^+$	$\text{pH} = -0.37 + 0.333 \log \frac{[HTeO_2^+]}{Te^{4+}}$
t.17.	$HTeO_2^+ \rightarrow TeO_2 + H^+$	$\text{pH} = -2.07 - \log[HTeO_2^+]$
t.18.	$TeO_3^{2-} + H_2O \rightarrow HTeO_4^- + H^+ + 2e^-$	$E^0 = 0.584 - 0.0295 \text{ pH} + 0.0295 \log \frac{[HTeO_4^-]}{TeO_3^{2-}}$
t.19.	$TeO_2 + H_2O \rightarrow TeO_3^{2-} + 2H^+$	$\text{pH} = 10.355 + 0.5 \log[TeO_3^{2-}] \rightarrow \text{anhydrous } TeO_2$ $\text{pH} = 7.545 + 0.5 \log[TeO_3^{2-}] \rightarrow \text{hydrous } TeO_2 \cdot H_2O$
t.20.	$Bi^{3+} + H_2O \rightarrow BiOH^{2+} + H^+$	$\text{pH} = 2.00 + \log \frac{[BiOH^{2+}]}{[Bi^{3+}]}$
t.21.	$HTeO_4^- \rightarrow TeO_4^{2-} + H^+$	$\text{pH} = 10.38 + \log \frac{[TeO_4^{2-}]}{[HTeO_4^-]}$
t.22.	$2BiOH^{2+} + H_2O \rightarrow Bi_2O_3 + 4H^+$	$\text{pH} = 2.98 - 0.5 \log[BiOH^{2+}]$
t.23.	$TeO_2 + 2H_2O \rightarrow TeO_3 + 2H^+ + 2e^-$	$E^0 = 1.020 - 0.0591 \text{ pH}$
t.24.	$Te^{4+} + 4H_2O \rightarrow H_2TeO_4 + 6H^+ + 2e^-$	$E^0 = 0.92 - 0.1773 \text{ pH}$
t.25.	$TeO_3^{2-} + H_2O \rightarrow TeO_4^{2-} + 2H^+ + 2e^-$	$E^0 = 0.892 - 0.0591 \text{ pH} + 0.0295 \log \frac{[TeO_4^{2-}]}{[TeO_3^{2-}]}$
t.26.	$HTeO_2^+ + 6H_2O \rightarrow TeO_3 + 3H^+ + 2e^-$	$E^0 = 0.953 - 0.0886 \text{ pH}$
t.27.	$2Bi_2O_3 + H_2O \rightarrow Bi_4O_7 + 2e^- + 2H^+$	$E^0 = 1.338 - 0.0591 \text{ pH}$
t.28.	$Bi_4O_7 + H_2O \rightarrow 2Bi_2O_4 + 2e^- + 2H^+$	$E^0 = 1.541 - 0.0591 \text{ pH}$
t.29.	$Bi_2O_4 + H_2O \rightarrow Bi_2O_5 + 2e^- + 2H^+$	$E^0 = 1.607 - 0.0591 \text{ pH}$
t.30.	$4BiOH^{2+} + 3H_2O \rightarrow Bi_4O_7 + 2e^- + 10H^+$	$E^0 = 2.042 - 0.2955 \text{ pH} - 0.1182 \log[BiOH^{2+}]$
t.31.	$2Bi^{3+} + 5H_2O \rightarrow Bi_2O_5 + 4e^- + 10H^+$	$E^0 = 1.759 - 0.1477 \text{ pH} - 0.0295 \log[Bi^{3+}]$
t.32.	$2H_2Te \rightarrow Te_2^{2-} + 4H^+ + 2e^-$	$E^0 = 0.638 - 0.1182 \text{ pH} + 0.0295 \log \frac{[Te_2^{2-}]}{[H_2Te]^2}$
t.33.	$TeO_2 + H_2O \rightarrow HTeO_3^- + H^+$	$\text{pH} = +12.96 + \log[HTeO_3^-] \rightarrow \text{anhydrous } TeO_2$ $\text{pH} = +7.34 + \log[HTeO_3^-] \rightarrow \text{hydrous } TeO_2 \cdot H_2O$
t.34.	$Bi_2Te_3 + 12H_2O \rightarrow 3HTeO_3^- + Bi_2O_3 + 18e^- + 21H^+$	$E^0 = -0.63 - 0.0098 \log[HTeO_3^-] + 0.0688 \text{ pH}$
t.35.	$HTeO_3^- + H_2O \rightarrow HTeO_4^{2-} + 2H^+ + 2e^-$	$E^0 = 0.813 - 0.0591 \text{ pH} + 0.0295 \log \frac{[HTeO_4^{2-}]}{[HTeO_3^-]}$
t.36.	$HTeO_3^- \rightarrow TeO_3^{2-} + H^+$	$\text{pH} = 7.74 + \log \frac{[TeO_3^{2-}]}{[HTeO_3^-]}$

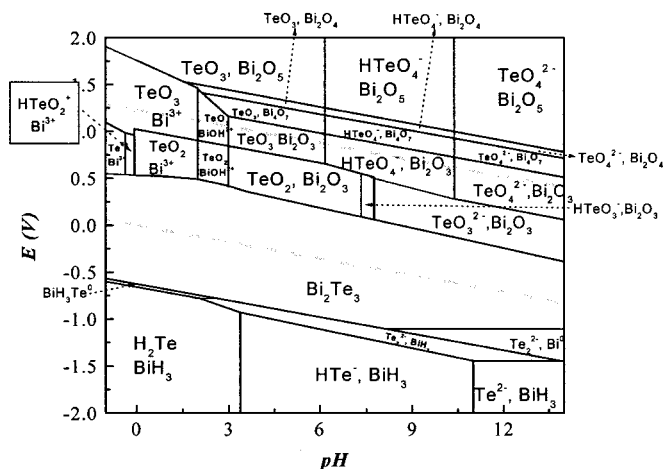


Figure 1. Pourbaix-type diagram for the electrodeposition of Bi and Te (at 25°C, 1 atm, and $\text{Bi} = 0.75 \times 10^{-2} \text{ M}$ and $\text{Te} = 1 \times 10^{-2} \text{ M}$) showing the thermodynamic stability of the dominant species as a function of potential and pH.

M final concentration. In this way, H^+ acts as supporting electrolyte and NO_3^- is the only counter ion. Tellurium powder was obtained from Alfa Aesar (99.9998%) and bismuth pieces from Mallinckrodt (99.8%). All glassware was cleaned in a base bath and thoroughly washed with doubly distilled water. In order to establish the influence of the cations in the electrodeposition process, concentrated Bi^{3+} and HTeO_2^+ solutions in 1 M HNO_3 were added in successive aliquots in separate experiments to a 1 M HNO_3 Te/Bi solution with initial concentrations of 1×10^{-2} and $0.75 \times 10^{-2} \text{ M}$, respectively. Also, concentrated HNO_3 was added to the solution to study the influence of changing pH.

Electrodepositions were carried out potentiostatically using an EG&G PAR model 273 potentiostat/galvanostat. We fabricated Pt working electrodes by sputter depositing approximately 500 nm of Cr and 2800 nm of Pt onto a quartz slide with a RANDEX, Perkin Elmer model 2400. The area of the working electrode was 1 cm^2 . The counter electrode was platinum gauze attached to a Pt wire and the reference electrode was silver/silver chloride (also known as SSCE). The electrodepositions were carried out at different potentials ($-0.12 < E < -0.52 \text{ V vs. SSCE}$) for 1 h each. The temperature was controlled by immersing the cell in an ice bath. This fixed the temperature at 2°C as measured by a thermometer in the electrodeposition cell.

The composition and morphology of the films were analyzed using several techniques: electron probe microanalysis (EPMA, Cameca SX-51) calibrated with tellurium (99.99%) and bismuth (99.9999%) standards; XRD (Siemens D5000, Cu $K\alpha$ radiation); and SEM, using a JEOL 6300.

Results and Discussion

As described below, the Pourbaix diagram calculated for Te ($1 \times 10^{-2} \text{ M}$) and Bi ($0.75 \times 10^{-2} \text{ M}$) at 25°C (Fig. 1) shows that pH -0.07 is optimal for the electrodeposition of Bi_2Te_3 for these concentrations. CV studies conducted at $\text{pH} < 0$ reveal that it is possible to obtain the desired phase over a relatively large range of potentials, but there are two different processes that occur depending on potential. Moreover, as shown below, the crystallinity and composition of Bi_2Te_3 films depend on the electrodeposition potential.

Pourbaix diagram.—We were interested in the range of conditions over which it is possible to electrodeposit Bi_2Te_3 , as well as the oxidizing and reducing abilities of the major stable species of Bi and Te in an aqueous solution at different pH and potentials. In

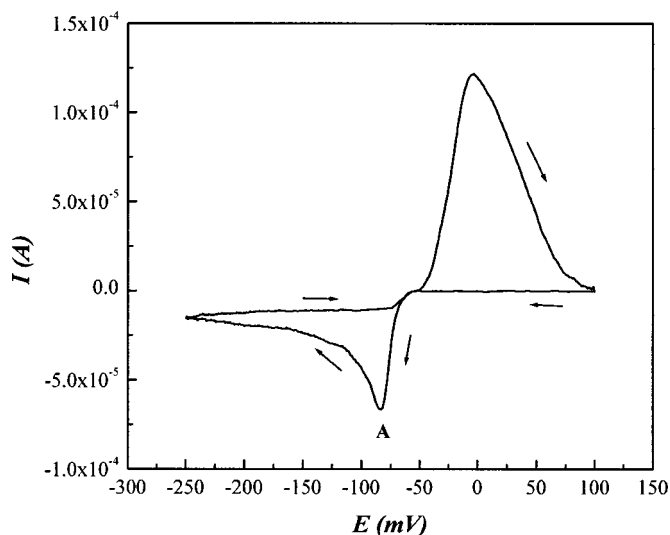


Figure 2. Cyclic voltammogram of Bi^{3+} ($0.75 \times 10^{-2} \text{ M}$) in 1 M HNO_3 . Scan rate = 0.01 V/s^{-1} , reference electrode Ag/AgCl (3 M NaCl), room temperature.

particular, we wanted to find the range of pH over which it is possible to dissolve both bismuth and tellurium such that they can be reduced to form Bi_2Te_3 . As is evident from Fig. 1, Bi_2Te_3 can be formed directly by the reduction of its cations and is stable over the entire range of pH as a bulk material, at potentials more negative than 0.5 V vs. NHE. Consequently, the choice of pH is determined solely by the solubility of tellurium and bismuth.

Tellurium is soluble as HTeO_2^+ in a narrow range at low pH ($-0.37 < \text{pH} < -0.07$) for a Te concentration of 10^{-2} M , (Eq. t.16 and t.17, Table I), and also at higher pH as HTeO_3^- ($\text{pH} > 12.96 + \log[\text{HTeO}_3^-]$ for tellurous anhydride (TeO_2) or $\text{pH} > 7.34 + \log[\text{HTeO}_3^-]$ for tellurous acid (H_2TeO_3 or $\text{TeO}_2 \cdot \text{H}_2\text{O}$), see Eq. t.33, Table I). In the range of pH from -0.07 to 5.34, a solution of 10 mM tellurium precipitates as TeO_2 , so if acidic solutions are used, the pH needs to be very carefully controlled. At pH lower than -0.37 , the stable species for this concentration is Te^{+4} . For lower tellurium concentrations in solution, the pH can be raised, see Eq. t.17 Table I, and the deposition rate will be lower. For example, for a 0.1 mM tellurium solution, the pH in which TeO_2 appears is 1.93.

Bismuth is soluble as BiOH^{2+} , but only for $\text{pH} < 4$ (see Eq. t.22, Table I). At higher pH, bismuth precipitates as Bi_2O_3 . The stable species for Bi at $\text{pH} < 2$ is Bi^{3+} . Therefore, in order to dissolve both tellurium and bismuth, it is necessary to work at a pH below -0.07 V vs. NHE . Under these conditions, tellurium is stable as HTeO_2^+ and bismuth as Bi^{3+} . Since the working pH has to be approximately zero in order to dissolve enough of the cationic species of both metals, a 1 M HNO_3 solution was used to dissolve elemental Bi and Te. These conditions are consistent with reports by others who have used acidic solutions for Bi_2Te_3 electrodeposition.¹⁷⁻²⁵ However, in our case it is not possible to use $\text{pH} \ll 0$ for this study because our ultimate goal is to understand the mechanism of electrodeposition of Bi_2Te_3 nanowires into porous alumina templates.²⁸ Porous Al_2O_3 membranes dissolve in very acidic baths.

Cyclic voltammograms.—CVs of solutions of (i) Bi^{3+} ($0.75 \times 10^{-2} \text{ M}$), (ii) HTeO_2^+ ($1 \times 10^{-2} \text{ M}$), and (iii) HTeO_3^- ($1 \times 10^{-2} \text{ M}$) with Bi^{3+} ($0.75 \times 10^{-2} \text{ M}$) in 1 M HNO_3 , were used to study the deposition mechanism reactions and to find the appropriate potential range for deposition.

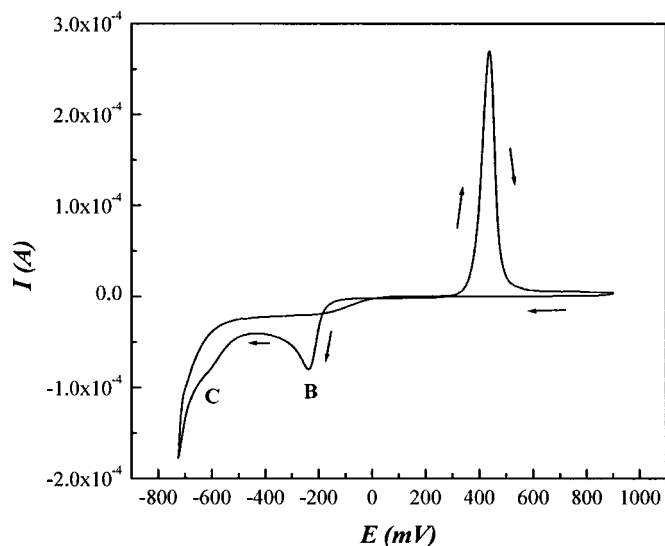
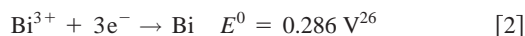


Figure 3. Cyclic voltammogram of HTeO_2^+ (1×10^{-2} M in 1 M HNO_3). Scan rate = 0.01 V/s^{-1} , reference electrode Ag/AgCl (3 M NaCl), room temperature.

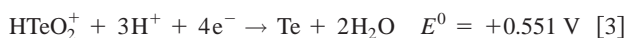
Bismuth cyclic voltammetry.—The CV observed for a solution containing Bi^{3+} (0.75×10^{-2} M) dissolved in HNO_3 is shown in Fig. 2. One reduction wave (labeled as peak A) is observed during the cathodic scan with $E_{\text{pc}} \approx -80 \text{ mV}$, and one oxidation wave is observed during the anodic scan with $E_{\text{pa}} \approx 0 \text{ mV}$. After applying potentials more negative than *ca.* -75 mV , a dark deposit formed on the working electrode. The identity of the deposit was determined to be elemental Bi by XRD. Therefore, we assigned peak A as the reduction of Bi^{3+} to Bi according to the following reaction



The anodic wave is assigned to the reverse of this reaction. These data are in good agreement with those observed by Magri *et al.*²³

Tellurium cyclic voltammetry.—The electrochemical behavior of tellurium is more complicated both because the formal oxidation state of the element can vary from Te^{6+} to Te^{2-} and because adsorption can play a large role due to the strong interactions between Te species and noble metals. The CV observed for solutions containing HTeO_2^+ (1×10^{-2} M) dissolved in HNO_3 is shown in Fig. 3. Two reduction waves (labeled as peaks B and C) are observed in the cathodic scan with $E_{\text{pc}} \approx -240$ and -600 mV , respectively. There is another wave at more negative potentials $< -700 \text{ mV}$, which is due to the onset of hydrogen evolution. There is only one oxidation wave with $E_{\text{pa}} \approx +440 \text{ mV}$.

After applying potentials more negative than *ca.* -190 mV , a deposit forms on the working electrode. The identity of the deposit was determined to be elemental Te by XRD. Therefore, we assigned peak B to the reduction of HTeO_2^+ to Te according to the following reaction



This assignment is consistent with previous reports.²⁹

The assignment of the process associated with peak C is less straightforward. We considered two processes: the direct reduction of Te(IV) to Te(-II), Reaction 4; and the reduction of Te(0) produced in the process associated with peak B to Te(-II), Reaction 5. The stable species under our experimental conditions is H_2Te (see Fig. 1, the Pourbaix diagram). In order to decide between these possibilities, we compared the thermodynamic values for the two reduction reactions

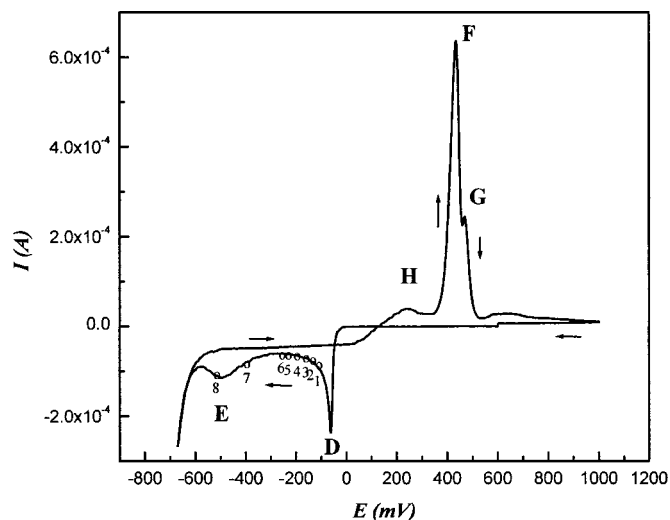
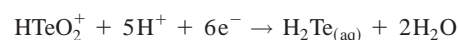
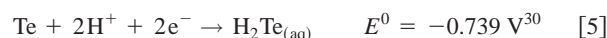


Figure 4. Cyclic voltammogram of Bi^{3+} (0.75×10^{-2} M) and HTeO_2^+ (1×10^{-2} M) in HNO_3 1 M. Scan rate = 0.01 V/s^{-1} , reference electrode Ag/AgCl (3 M NaCl), room temperature. (O) Correspond to potentials in which electrodeposition of films has been carried out.

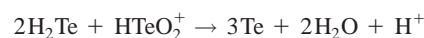


$$E^0 = +0.121 \text{ V}^{30} \quad [4]$$



The positive E^0 for Reaction 4 indicates that the reduction of HTeO_2^+ in solution to H_2Te is more favorable than the reduction to Te^0 . Therefore, we assigned peak C to Reaction 4. It is notable that the experimental difference between the peak reduction potentials for the two oxidation waves (peaks B and C) agrees reasonably well with the difference in calculated values, ΔE^0 , for Reactions 3 and 4. The experimental and calculated values are 0.43 and 0.36 V, respectively.

While Reaction 4 accounts for the electrochemical reduction associated with peak C, this reaction cannot account for the entire process. We do not observe the evolution of gaseous H_2Te . However, if the amounts generated were very small, and considering that H_2Te is expected to decompose quickly, there would not necessarily be bubbles large enough to be observed. H_2Te ($\Delta G_f^\circ = 142.7 \text{ kJ/mol}$) is not stable in acid solutions in the presence of HTeO_2^+ ($\Delta G_f^\circ = -261.54 \text{ kJ/mol}$). It is likely that the following chemical reaction occurs as soon as H_2Te is generated electrochemically.



$$\Delta G_f^\circ = -498.118 \text{ kJ/mol} \quad [6]$$

This reaction is energetically favorable, and has been described previously in the literature as an additional pathway for Te^0 deposition.^{31,32} Therefore, we propose that the net process associated with peak C is the reduction of HTeO_2^+ by a two-step reaction involving the electrochemical generation of H_2Te as an intermediate (Reaction 4) and the net deposition of elemental Te by a subsequent chemical reaction (Reaction 6). The overall process behaves as a four-electron reduction from HTeO_2^+ to Te^0 (equivalent to Reaction 3). The six-electron reduction has been observed only for low HTeO_2^+ concentrations ($< 10^{-3} \text{ M}$).³³

There are several other pieces of evidence to support the claim that the processes associated with both peaks B and C lead to the deposition of Te. First, we have verified by XRD diffraction that

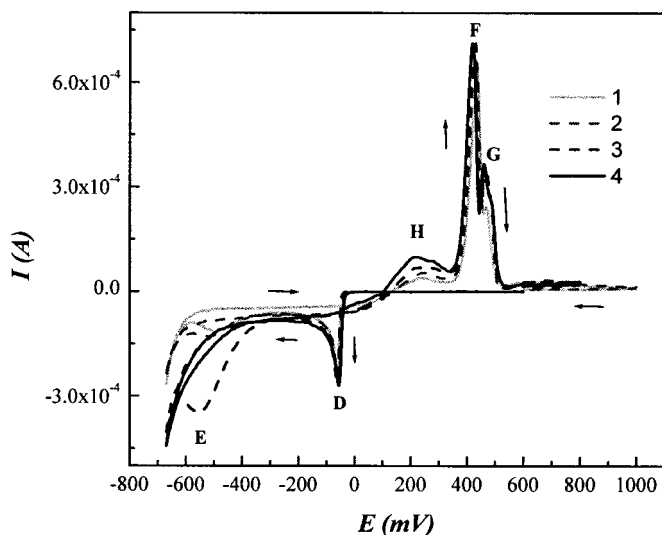


Figure 5. Voltammograms in HNO_3 1 M of Bi^{3+} (0.75×10^{-2} M) and HTeO_2^+ (1×10^{-2} M). (1) Aliquots of a concentrated Bi^{3+} in 1 M HNO_3 solution were added: (2) 0.2 mL, (3) 0.4 mL, and (4) 0.8 mL. Scan rate = 0.01 V/s^{-1} , room temperature.

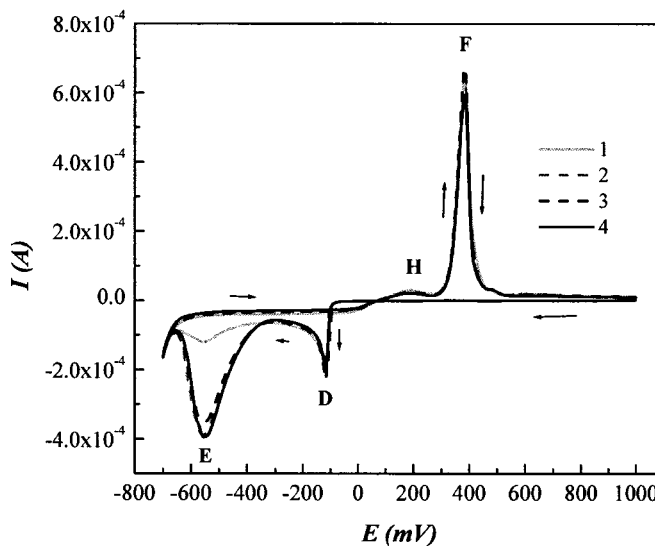


Figure 6. Voltammograms in HNO_3 (1) 1 M of Bi^{3+} 0.75×10^{-2} M and HTeO_2^+ 1×10^{-2} M, (1) Aliquots of a concentrate HTeO_2^+ in 1 M HNO_3 solution were added: (2) 0.2 mL, (3) 0.4 mL, and (4) 0.8 mL. Scan rate = 0.01 V/s^{-1} , room temperature.

deposits of Te persist on the electrode even after applying potentials more negative than -600 mV . Second, the observation of one oxidation wave ($E_{\text{pa}} \approx +440 \text{ mV}$) indicates that there is only one reduction product. We have assigned this oxidation wave to the reverse of Reaction 3. Finally, upon sweeping the potential in the anodic direction, a nucleation loop is observed around -100 mV . The large separation between the cathodic and the anodic waves indicates that the tellurium deposition reaction is irreversible.

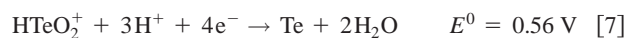
We conclude that the deposition of Te is favorable at potentials more negative than *ca.* -190 mV , but the mechanism of deposition changes once the potential is more negative than -600 mV . We suggest that Te deposits are stabilized in acid even at very negative potentials by the presence of the oxidizing agent HTeO_2^+ .

Bi-Te cyclic voltammetry.—The CV observed for a solution containing both HTeO_2^+ ($1 \times 10^{-2} \text{ M}$) and Bi^{3+} ($0.75 \times 10^{-2} \text{ M}$) dissolved in HNO_3 is shown in Fig. 4. As was observed for solutions containing only HTeO_2^+ , two reduction waves (labeled as peaks D and E) are observed in the cathodic scan with $E_{\text{pc}} \approx -62$ and -500 mV , respectively. There is another wave at more negative potentials $< -600 \text{ mV}$, which is due to the onset of hydrogen evolution. There is one major oxidation wave with $E_{\text{pa}} \approx +430 \text{ mV}$ (labeled as peak F). The latter wave has a small shoulder with $E_{\text{pa}} \approx +440 \text{ mV}$ (labeled as peak G). There is also a minor oxidation wave at less positive potentials (labeled as peak H).

The potential at which reduction is observed when both HTeO_2^+ and Bi^{3+} are present in solution ($E_{\text{pc}} \approx -62 \text{ mV}$) is more positive compared with the reduction of solutions containing only HTeO_2^+ ($E_{\text{pc}} \approx -240 \text{ mV}$) or only Bi^{3+} ($E_{\text{pc}} \approx -80 \text{ mV}$) for comparable concentrations. This behavior is due to the formation of a compound on the surface of the electrode, which shifts the potentials. This process is known as mutually induced codeposition mechanism,³⁴ autoregulation, or pure underpotential deposition (UPD) and corresponds to Class II compounds of the induced codeposition mechanism as described by Kröger.³⁴ This type of deposition occurs when the two reversible (Nernst) potentials for the two separate cations are closer than $\sim 250 \text{ mV}$ and the free energy of formation of the compound provides a sufficient decrease in the anodic terms in the Butler-Volmer equations. Under these conditions, the cathodic components cause net deposition of both elements, at comparable rates, at more positive potential of where either element deposits

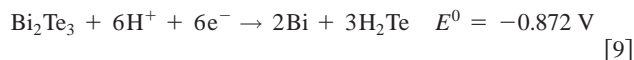
individually.³⁵ After applying potentials more negative than *ca.* -50 mV , a deposit forms on the working electrode. The identity of the deposit is determined to be Bi_2Te_3 by XRD; elemental Bi and elemental Te are not detected in the XRD pattern. Therefore, we assign peak D as the reduction of HTeO_2^+ and Bi^{3+} to Bi_2Te_3 according to the general reaction, Reaction 1, when $\Delta G_f^\circ = -899.088 \text{ kJ/mol}$. The direct deposition of Bi_2Te_3 instead of the codeposition of Bi(s) and Te(s) is consistent with the negative free energy of formation for Bi_2Te_3 and with the Pourbaix diagram in Fig. 1. This reaction is consistent with the general equation that has been reported in previous work.^{19,20}

In order to learn more about the process by which Bi_2Te_3 is deposited, we examined the effects of variations in the concentrations of Bi^{3+} and HTeO_2^+ on the CVs. Aliquots of a concentrated Bi^{3+} solution (in 1.00 M HNO_3) were added successively to a solution with initial concentrations of $1 \times 10^{-2} \text{ M}$ HTeO_2^+ and $0.75 \times 10^{-2} \text{ M}$ Bi^{3+} . After each addition, the CVs shown in Fig. 5 were recorded. A similar series of CVs were recorded after successive additions of a concentrated HTeO_2^+ solution (in 1.00 M HNO_3) to the same stock solution as shown in Fig. 6. The potential at which the reduction peaks occur as well as the peak currents do not change significantly after successive additions of either Bi^{3+} (see Fig. 5) or the addition of HTeO_2^+ (see Fig. 6). That would imply that the current depends on the species adsorbed onto the electrode surface. It is also noticeable that there is a sharp increase in current at the deposition potential for Bi_2Te_3 . This suggests that the reduction is associated with a species adsorbed onto the electrode surface. Indeed, previous studies have shown that HTeO_2^+ adsorbs strongly onto Pt electrodes.³³ For these reasons, we propose that the first step in the deposition process involves the reduction of HTeO_2^+ adsorbed onto the electrode to produce Te and this triggers the reduction of Bi^{3+} as follows



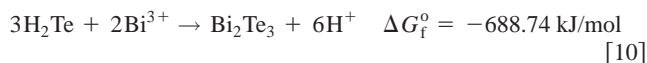
The deposition takes place by the electrochemically induced reduction of HTeO_2^+ and the reaction with Bi^{3+} . A similar two-step deposition mechanism has been proposed previously for the deposition of others tellurides and selenides.³⁶⁻⁴¹

There is a second peak (peak E with $E_{pc} \approx -500$ mV) in the CV for the deposition of Bi_2Te_3 , as shown in Fig. 4. As was the case for the second peak observed for solutions containing only HTeO_2^+ , the assignment of this peak is not straightforward. Again, we can consider two processes, the direct reduction of HTeO_2^+ to H_2Te and the reduction of the product of the process associated with peak D (in this case, Bi_2Te_3) to H_2Te . In order to decide between these possibilities, we compared the thermodynamic values for the two reduction reactions, Reaction 4 plus



The reduction of Bi_2Te_3 to H_2Te is less favorable than the reduction of HTeO_2^+ to H_2Te . On the basis of these thermodynamic calculations, we associate peak E with the direct reduction of HTeO_2^+ to H_2Te since this has to occur at lower potentials than the reduction of Bi_2Te_3 to H_2Te . This is the same assignment as for peak C, when only HTeO_2^+ is present.

As was the case for peak C, Reaction 4 cannot account for the entire process associated with peak E since H_2Te ($\Delta G_f^0 = +142.7$ kJ/mol) is not stable in acidic solutions in the presence of Bi^{3+} . Instead, Bi_2Te_3 ($\Delta G_f^0 = -77$ kJ/mol) is produced as soon as H_2Te is generated, according to the following chemical reaction



This reaction is consistent with the fact that no bubbles (evolution of gaseous H_2Te) are observed during the CVs. So the net process associated with peak E is the reduction of HTeO_2^+ by a two-step reaction involving the electrochemical generation of H_2Te as an intermediate and the deposition of Bi_2Te_3 by a subsequent chemical reaction. We have verified that deposits of Bi_2Te_3 persist on the electrode even after applying potentials more negative than -500 mV.

Peak C for solutions containing only HTeO_2^+ and peak E for solutions containing both Bi^{3+} and HTeO_2^+ are assigned to the same electrochemical process (the six-electron reduction of HTeO_2^+). However, when Bi^{3+} is present, Bi_2Te_3 is formed in the subsequent reaction instead of Te. The driving force for the formation of Bi_2Te_3 is the greater stability of the compound ($\Delta G_f^0 = -688.74$ kJ/mol, Reaction 10) vs. Te ($\Delta G_f^0 = -498.118$ kJ/mol, Reaction 6). It is notable that the potential for peak E ($E_{pc} \approx -500$ mV) is more positive compared with the potential for peak C ($E_{pc} \approx -600$ mV). We attribute this difference to the formation of the compound. We conclude that the overall process for peak E is again the result of Reaction 1. However, this general equation is explained by a different electrodeposition mechanism. A similar mechanism has already been proposed for CdTe.³⁵

As shown in Fig. 5, upon addition of Bi^{3+} there is a shift in the potential to more negative values. If this process were due to the reduction of Bi^{3+} , then we would expect a potential shift in the opposite direction, to more positive values. However, since by increasing the concentration of Bi^{3+} there is relatively less HTeO_2^+ available to deposit, a shift to more negative potentials is reasonable. An increase in the current density is also observed.

In order to verify the effect of the pH, concentrated HNO_3 was added to the stock solution of Bi^{3+} and HTeO_2^+ (see Fig. 7). There are no changes in any of the waves, but the current associated with the second reduction wave increases.

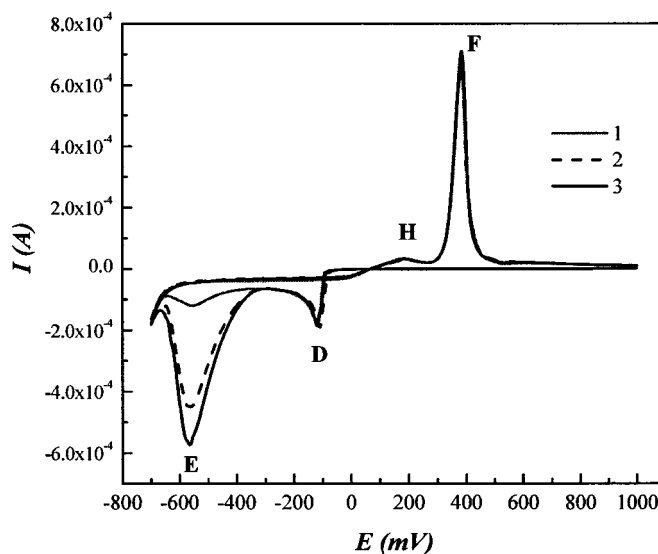
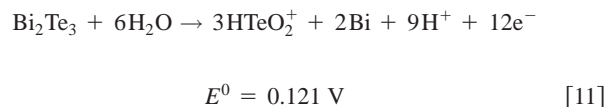


Figure 7. Voltammograms in HNO_3 1 M of Bi^{3+} 0.75×10^{-2} M and HTeO_2^+ 1×10^{-2} M. (1) Aliquots of a concentrate HNO_3 were added: (2) 0.1 mL, and (3) 0.2 mL. Scan rate = 0.01 V/s^{-1} , room temperature.

Because the processes associated with both peaks D and E lead to deposition of Bi_2Te_3 , we expect to see only the oxidation of Bi_2Te_3 on the reverse scan. The sharp increase in current associated with the oxidation wave labeled F ($E_{pa} \approx +430$ mV) and the shoulder labeled G ($E_{pa} \approx +440$ mV) indicate that these waves correspond to the oxidation of a deposit on the electrode surface. These two closely spaced peaks suggest that the oxidation of Bi_2Te_3 occurs via two steps



followed by Reaction 2. The total reaction is again the reverse of Reaction 1. The oxidative process can therefore be described as an oxidation of Bi_2Te_3 to HTeO_2^+ (wave F, Reaction 11), followed by an oxidation of Bi to Bi^{3+} (Reaction 2).

Two possible explanations for wave G are (1) the oxidation of Bi from Bi_2Te_3 following the oxidation of Te in Peak F or (2) the oxidation of a stable layer on the surface of the electrode. Upon addition of Bi^{3+} to the solution, the area associated with peak G increases relative to peak F, as shown in Fig. 5. This is consistent with the first explanation for peak G as the oxidation of Bi from Bi_2Te_3 . The observation of a relatively larger current associated with peak G compared with peak F upon addition of Bi^{3+} suggests that the deposits prepared in solutions relatively rich in Bi contain more Bi. According to the phase diagram, excess Bi can be incorporated into the structure.⁴² We provide further evidence that films of Bi-rich Bi_2Te_3 can be electrodeposited in the next section. We note also that previous work has shown that when Bi^{3+} is a limiting reagent, Te inclusions are likely to form.³³ However, it is a bit unusual that the compound decomposes in two steps. We might expect that both elements would be oxidized simultaneously since they were deposit into a compound. An alternative explanation is that peak F is associated with the complete oxidation of Bi_2Te_3 . If both Bi and Te are stripped from the electrode simultaneously, then peak G could be explained as the oxidation of a stable layer that is formed on the surface of the electrode due to a UPD process. How-

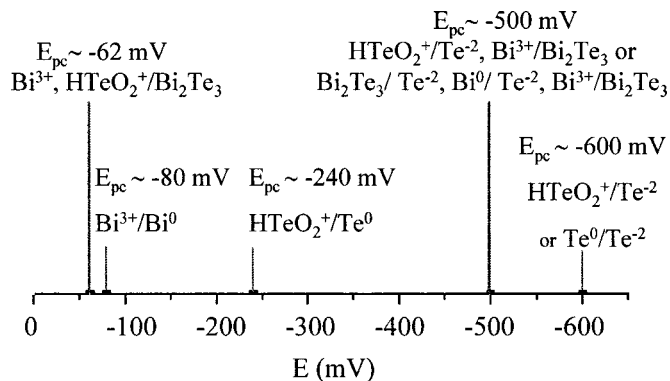


Figure 8. Summary of the reduction potentials observed as determined by the cyclic voltammogram studies.

ever, since this second explanation does not account for the increase in intensity of peak G upon addition of Bi^{3+} to the solution, we favor the first explanation.

The small peak labeled H ($E_{\text{pa}} \approx +220$ mV) is a minor oxidation step. The amount of current passed for this oxidation increases upon addition of Bi^{3+} to the solution (Fig. 5), but remains unchanged upon addition of HTeO_2^+ (Fig. 6) or H^+ (Fig. 7). Therefore,

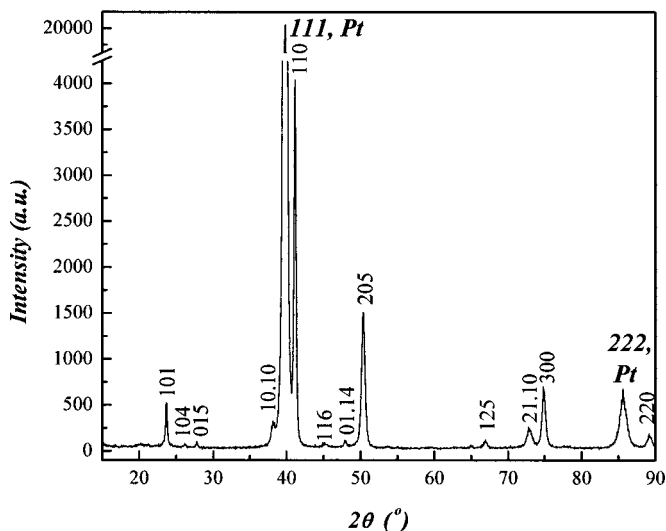


Figure 10. X-ray diffraction pattern of a Bi_2Te_3 sample (mark with Miller indices, PCPDF 15-0863) obtained from Bi^{3+} 0.75×10^{-2} M and HTeO_2^+ 1×10^{-2} M in HNO_3 1 M solution using Pt on quartz as a substrate (mark with Miller indices, PCPDF 04-0802). Note that the intensity axis has been broken because of the strong orientation of the substrate along the 111 direction. The films are oriented along the 110 direction.

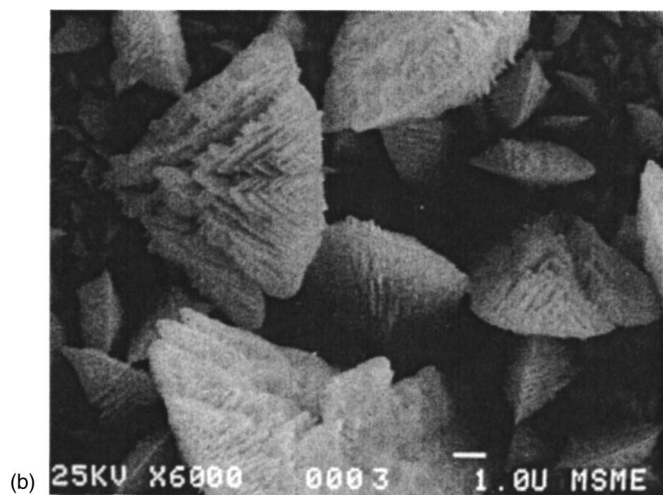
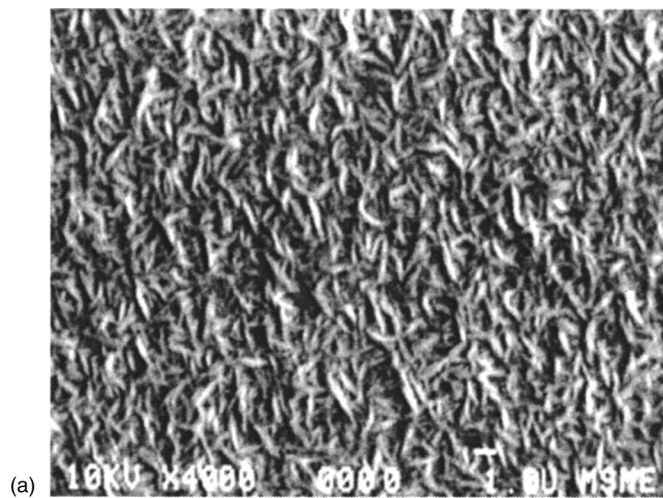


Figure 9. SEM micrographs of two examples of the types of morphology that can be observed under (a) slow and (b) fast deposition conditions.

it is likely that peak H is associated with the oxidation of Bi. Since this oxidation occurs at less cathodic potentials than the oxidation of bulk Bi_2Te_3 , we propose that this oxidation is due to the top layer of Bi on the Bi_2Te_3 film. This is consistent with the processes we have identified for the deposition of Bi_2Te_3 , which involve the reduction of HTeO_2^+ followed by a reaction with Bi^{3+} . This should place Bi on the top layer. Moreover, the structure of Bi_2Te_3 can accommodate excess Bi by incorporating layers between the main Te-Bi-Te-Bi-Te layers of the hexagonal unit cell (adjoining layers are bound by van der Waals' interactions).⁴³ Thus, the increase in current associated with peak H upon addition of excess Bi^{3+} may be due to an increase in the amount of Bi in the top layer.

A summary of the electrochemical and chemical processes that occur as a function of potential for solutions containing Bi^{3+} , HTeO_2^+ , and a mixture of the two are shown in Fig. 8. Proposed processes for the electrochemical reactions are also shown. We conclude that the deposition of Bi_2Te_3 is favorable at potentials more negative than *ca.* -50 mV vs. Ag/AgCl on Pt as a working electrode, but a new process for deposition appears once the potential is more negative than *ca.* -500 mV.

Film deposition and characterization.—Electrodepositions of Bi_2Te_3 films were carried out on platinum electrodes from -0.12 to -0.52 V vs. Ag/AgCl (3M NaCl) for 1 h each at 2°C . The deposition at 2°C seems to give more homogenous films than the ones obtained at room temperature. After a few seconds a deposit appeared on the electrode. In all of the cases a nearly perfect stoichiometry was found for a large range of potentials. This can be explained because neither element can be electrodeposited individually. For that reason, a “feedback” exists (through increasing anodic terms and immediate dissolution of any element in excess of that required by the equilibrium constant-mass action law $a_{\text{MX}}/a_{\text{M}}a_{\text{X}} = \exp[-\Delta G_{\text{MX}}^0/RT]$), which ensures nearly perfect MX stoichiometry over a broad potential range as determined by theoretical modeling and computer simulation.³⁵ The appearance of the deposit varied with potential. For potentials near -0.12 V (vs. Ag/AgCl), the deposit appeared gray and very smooth by eye. A representative SEM image, for a typical film grown around those potentials, is shown in Fig. 9a. The feature sizes are on the order of $2.5 \times 0.25 \mu\text{m}$. We attribute the smoothness of the film, the uniform-

Table II. Atomic percentages as a function of the applied potential (vs. Ag/AgCl (3 M NaCl)) for depositions on Pt electrodes calculated from electron probe microanalysis. The concentration of the solution is HTeO_2^+ (1×10^{-2} M) and Bi^{3+} (0.75×10^{-2} M) in 1 M HNO_3 . Deposition time, 60 min except for the $E = -0.52$ in which the growth was so fast that a thick film formed in only 20 min. The 8 samples shown correspond with the 8 points on Fig. 4.

E applied	[Bi] electrode %	[Te] electrode %	Formula as solid solution	Composition with the closet match from the phase diagram	Phase
-0.12	39.2	60.8	$\text{Bi}_{1.96}\text{Te}_{3.04}$	$\text{Bi}_{1.99}\text{Te}_{3.01}$	Bi_2Te_3
-0.145	39.6	60.4	$\text{Bi}_{1.98}\text{Te}_{3.02}$	$\text{Bi}_{1.99}\text{Te}_{3.01}$	Bi_2Te_3
-0.17	43.9	56.1	$\text{Bi}_{2.19}\text{Te}_{2.81}$	$\text{Bi}_{2.22}\text{Te}_{2.78}$	Bi_4Te_5
-0.195	45.3	54.7	$\text{Bi}_{2.26}\text{Te}_{2.74}$	$\text{Bi}_{2.22}\text{Te}_{2.78}$	Bi_4Te_5
-0.22	47.7	52.3	$\text{Bi}_{2.38}\text{Te}_{2.62}$	$\text{Bi}_{2.31}\text{Te}_{2.69}$	Bi_6Te_7
-0.26	57.4	43.6	$\text{Bi}_{2.87}\text{Te}_{2.13}$	$\text{Bi}_{2.85}\text{Te}_{2.145}$	Bi_4Te_3
-0.42	45.9	54.1	$\text{Bi}_{2.29}\text{Te}_{2.71}$	$\text{Bi}_{2.22}\text{Te}_{2.78}$	Bi_4Te_5
-0.52	44.1	55.9	$\text{Bi}_{2.20}\text{Te}_{2.80}$	$\text{Bi}_{2.22}\text{Te}_{2.78}$	Bi_4Te_5

mity, the preferred orientation along $\langle 110 \rangle$ (as detected by XRD, Fig. 10) to slow growth. At more cathodic potentials the films appear black. The feature sizes are on the order of $2 \times 0.1 \mu\text{m}$ which are part of a more complex structure on the order of $5 \times 5 \mu\text{m}$. As shown in the SEM image in Fig. 9b for a typical film grown at more cathodic potentials, the films are much rougher. We attribute the smaller grain size and the rough morphology to faster growth. For $E \leq -500$ mV, the roughness can also be attributed to a change in electrodeposition mechanism. This is consistent with the relatively larger current observed for depositions at more cathodic potentials.

The phases of the films were determined by XRD. A representative powder pattern is shown in Fig. 10. All diffraction peaks observed can be attributed to either Bi_2Te_3 or the Pt substrate as indicated in the figure. The positions of the diffraction lines are consistent with Bi_2Te_3 for films grown at potentials close to -0.12 V vs. Ag/AgCl. Whereas the 015 diffraction peak is expected to be the most intense for randomly oriented polycrystalline Bi_2Te_3 samples according to the powder diffraction file for PC (PCPDF) 15-0863 ($R\bar{3}m$, $a = 4.385 \text{ \AA}$, $c = 30.48 \text{ \AA}$), the 110 peak is the largest in the diffraction pattern for the electrodeposited films. This 110 peak corresponds to the $\langle 110 \rangle$ orientation of the film, which means that the Te-Bi-Te layers are parallel to the substrate. Thus, we conclude the films are textured along the $\langle 110 \rangle$ direction. For films grown at more cathodic potentials, there are small shifts in the peak positions relative to Pt substrate peaks. This indicates that there is a change in film composition from the ideal Bi:Te stoichiometry of 2:3. Moreover, those films present a less strong $\langle 110 \rangle$ orientation.

The compositions of the films were determined by EPMA. A summary of the data obtained from films electrodeposited at eight different potentials is given in Table II. The optimal Bi:Te stoichiometry of 2:3 is achieved for depositions performed at $-0.12 < E < -0.145$ V vs. Ag/AgCl. However, upon increasing the potential to more negative values, $E > -0.17$ V vs. Ag/AgCl, the ratio of Bi:Te increases. A ratio of 4:5 (Bi_4Te_5) is observed for several films. Ratios as large as 4:3 (Bi_4Te_3) are observed. This kind of behavior is advantageous because only by changing the potential, the material composition can be manipulated to yield both the p-type (Bi-rich phases)²⁴ and n-type (stoichiometric Bi_2Te_3)²⁴ branches of a thermoelectric device or create multilayers of p- and n-type material by pulsing the potential.

The peak shifts observed in the XRD diffraction patterns and the compositions measured by EPMA are consistent with those reported for stacking variants of $\text{Bi}_{2+x}\text{Te}_{3-x}$.^{23,42} Excess Bi can be incorporated into Bi_2Te_3 by introducing a Bi layer between existing Te-Bi-Te-Bi-Te units. Such stacking variants or polytypoids are represented as $\text{Bi}_{2+x}\text{Te}_{3-x}$ (where $x = 1.5, 1.335, 0.855, 0.5, 0.31,$ and 0.22).⁴² Therefore, we conclude that as the deposition potential is made more negative, Bi-rich phases are obtained.

While Bi_2Te_3 can accommodate an excess of Bi,⁴² only small amounts of excess Te are found as antisite defects. Large excesses of Te result in the precipitation of pure Te.⁴⁰ For systems such as CdTe, Te metal inclusions have been found when depositions are performed under low Cd^{2+} concentrations and at very negative potentials.⁴⁰ We have not detected Te inclusions by XRD, and the microprobe analyses indicate that we do not have large excesses of Te in our films.

While we do not have Te inclusions in the bulk of the film (as detected by XRD), the film composition near the substrate is of particular concern. It has been observed for the electrodeposition of chalcogenides (such as CdTe) from M^{n+} and HTeO_2^+ electrochemical baths that the film near the substrate can be Te-rich if the initial interfacial concentration of HTeO_2^+ is greater than the steady-state value.³³ In addition, it seems to be a slight concentration gradient in Te at the base of electrodeposited nanowires of Bi_2Te_3 when the wires are grown quickly.⁴⁴

We conclude that if the concentration of Bi^{3+} in solution is too low or its diffusion too slow to complete Reaction 8, then we might expect to find Te inclusions in the Bi_2Te_3 deposits. On the other hand, if the concentration of Bi^{3+} is very high, then the Bi_2Te_3 deposits are Bi rich. Indeed, since HTeO_2^+ is adsorbed in the first step of the deposition process, the final composition of the alloy depends strongly on Bi diffusion. We have found that one set of conditions that lead to the deposition of stoichiometric films of Bi_2Te_3 is with an excess of HTeO_2^+ in solution compared with Bi^{3+} , and a potential that is not very negative. Specifically, we used HTeO_2^+ (1×10^{-2} M) and Bi^{3+} (0.75×10^{-2} M) in 1 M HNO_3 , and a deposition potential of -0.12 V vs. Ag/AgCl at 0°C .

Conclusion

The electrodeposition of Bi_2Te_3 is complex, involving two different processes depending on the applied potential. The deposition of Bi_2Te_3 is favorable at potentials negative of ca. -50 mV, but a new mechanism of deposition appears once the potential is more negative than ca. -500 mV. Furthermore, from the analyses of the CVs and the compositions of the resulting films, we conclude that when HTeO_2^+ is a limiting reagent, Bi-rich phases form.

Acknowledgments

The authors would like to thank Margaret Chan for her help in the synthesis of some Bi_2Te_3 films, Professor Jeffrey Long and his group for the use of the Bioanalytical Systems Basomatic CV50W, Ron Wilson (Department of Materials Science, UCB), Dr. Gordon Vrdoljak (Electron Microscope Lab, UCB), and John Donovan (Electron Probe Microanalysis Laboratory, UCB), and Microfabrication Laboratory for the use of RANDEX. M.S.M.G thanks MEC/

Fulbright Fellowship program. This work was funded by the U.S. Department of Defense ONR-MURI on Thermoelectrics, no. N00014-97-1-0516.

The University of California at Berkeley assisted in meeting the publication costs of this article.

References

1. E. J. Winder, A. B. Ellis, and G. C. Lisensky, *J. Chem. Educ.*, **73**, 940 (1996).
2. W. B. Gosney, *Principles of Refrigeration*; Chap 1, Cambridge University, Cambridge, U.K. (1982).
3. L. D. Hicks, T. C. Harman, X. Sun, and M. S. Dresselhaus, *Phys. Rev. B*, **53**, 10493 (1996).
4. L. D. Hicks and M. S. Dresselhaus, *Phys. Rev. B*, **47**, 16631 (1993).
5. L. D. Hicks and M. S. Dresselhaus, *Phys. Rev. B*, **47**, 12727 (1993).
6. T. C. Harman, P. J. Taylor, D. L. Spears, and M. P. Walsh, *J. Electron. Mater.*, **29**, L1 (2000).
7. T. C. Harman, D. L. Spears, and M. P. Walsh, *J. Electron. Mater.*, **28**, L1 (1999).
8. T. Koga, T. C. Harman, S. B. Cronin, and M. S. Dresselhaus, *Phys. Rev. B*, **60**, 14286 (1999).
9. S. Cho, A. DiVenere, G. K. Wong, J. B. Ketterson, and J. R. Meyer, *Phys. Rev. B: Condens. Matter*, **59**, 10691 (1999).
10. R. Venkatasubramanian, T. Colpitts, E. Watko, and J. Hutchby, in *Proceedings of the IEEE 15th International Conference on Thermoelectrics*, p. 454 (1996).
11. T. C. Harman, D. L. Spears, and M. J. Manfra, *J. Electron. Mater.*, **25**, 1121 (1996).
12. M. S. Dresselhaus, G. Dresselhaus, X. Sun, Z. Zhang, S. B. Cronin, and T. Koga, *Phys. Solid State*, **41**, 679 (1999).
13. M. S. Dresselhaus, T. Koga, X. Sun, S. B. Cronin, K. L. Wang and G. Chen, in *Proceedings of the 16th International Conference on Thermoelectrics, ICT '97*, IEEE, Vol. 16, p. 12, Aug 26-29, 1997.
14. A. Ioffe, *Semiconductors Thermoelements and Thermoelectricity Cooling*, Infosearch, London (1957).
15. B. Yim and F. Rosi, *Solid-State Electron.*, **15**, 1121 (1972).
16. <http://www.melcor.com/prop21C.htm>
17. M. Takahashi, Y. Oda, T. Oginio, and S. Furuta, *J. Electrochem. Soc.*, **140**, 2550 (1993).
18. J.-P. Fleurial, A. Borshchevsky, M. A. Ryan, W. H. Philips, J. G. Snyder, T. Caillat, E. A. Kolawa, J. A. Herman, P. Mueller, and M. Nicolet, *Mater. Res. Soc. Symp. Proc.*, **545**, 493 (1999).
19. J.-P. Fleurial, A. Borshchevsky, M. A. Ryan, E. A. Kolawa, T. Kacisch, and R. Ewell, in *Proceedings of the 16th International Conference on Thermoelectrics, ICT 97*, IEEE, Vol. 16, p. 641, Aug 26-29, 1997.
20. H. Chaoui, P. Magri, J. Bessieres, C. Boulanger, and J. J. Heizmann, *Mater. Sci. Forum*, **157-162**, 1371 (1994).
21. H. Chaoui, J. Bessieres, A. Modaresi, and J. J. Heizmann, *J. Appl. Electrochem.*, **30**, 419 (2000).
22. P. Magri, C. Boulanger, and J. M. Lecuire, *Electrodeposition of Bi₂Te₃ Films*, B. Mathiprakasam and P. Heenan, Editors, AIP Press, p. 277, Kansas City, MO (1994).
23. P. Magri, C. Boulanger, and J. M. Lecuire, *J. Mater. Chem.*, **6**, 773 (1996).
24. L. Huang, W. Wang, and M. C. Murphy, *Microsyst. Technol.*, **6**, 1 (1999).
25. S. A. Sapp, B. B. Lakshmi, and C. R. Martin, *Adv. Mater.*, **11**, 402 (1999).
26. M. Pourbaix, *Atlas of Electrochemical Equilibria in Aqueous Solutions*, Pergamon, New York (1966).
27. A. J. Bard, R. Parsons, and J. Jordan, *Standard Potentials in Aqueous Solutions*, Marcel Dekker, Inc., New York (1985).
28. A. L. Prieto, M. S. Sander, M. S. Martín-González, R. Gronsky, T. Sands, and A. M. Stacy, *J. Am. Chem. Soc.*, **123**, 7160 (2001).
29. M. P. R. Panicker, M. Knaster, and F. A. Kroger, *J. Electrochem. Soc.*, **125**, 566 (1978).
30. E. Deltombe and N. de Zoubov, *Tellur in Atlas d'Equilibres Electrochimiques a 25°C*, M. Pourbaix, Editor, p. 560, Gauthier-Villars, Paris (1963).
31. E. Mori, C. K. Baker, J. R. Reynolds, and K. Rajeshwar, *J. Electroanal. Chem.*, **252**, 441 (1988).
32. M. Traore, R. Modolo, and O. Vittori, *Electrochim. Acta*, **33**, 991 (1988).
33. W. J. Danaber and L. E. Lyons, *Aust. J. Chem.*, **37**, 689 (1984).
34. F. A. Kröger, *J. Electrochem. Soc.*, **125**, 2028 (1978).
35. R. D. Engelken, *J. Electrochem. Soc.*, **135**, 834 (1988).
36. E. Mori and K. Rajeshwar, *J. Electroanal. Chem.*, **258**, 415 (1989).
37. I. Zhdanov, *Encyclopedia of Electrochemistry of the Elements*, A. J. Bard, Editor, Vol. 4, Marcel Dekker, Inc., New York (1975).
38. K. K. Mishra and K. Rajeskman, *J. Electroanal. Chem.*, **273**, 169 (1989).
39. M. Takahashi, K. Uosaki, and H. Kita, *J. Appl. Phys.*, **55**, 3879 (1984).
40. F. A. Selim and F. A. Kroeger, *J. Electrochem. Soc.*, **124**, 401 (1977).
41. G. Maurin, O. Solorza, and H. Takenouti, *J. Electroanal. Chem.*, **202**, 323 (1986).
42. T. B. Massalski, H. Okamoto, P. R. Subramanian, L. Kacprzak, W. W. Scott, Jr., M. A. Fleming, R. Boring, and A. Losasso, *Binary Alloy Phase Diagrams, 2nd ed.*, ASM International Materials Park, OH (1990).
43. C. Sella, P. Boncorps, and J. Verdel, *J. Electrochem. Soc.*, **133**, 2043 (1986).
44. M. Sander, A. L. Prieto, Y. M. Lin, R. Gronsky, A. Stacy, T. Sands, and M. Dresselhaus, *Mater. Res. Soc. Symp. Proc.*, **635**, 36 (2000).